

PAPER • OPEN ACCESS

## Visualization of gold fiducial markers in the prostate using phase-cycled bSSFP imaging for MRI-only radiotherapy

To cite this article: Yulia Shcherbakova *et al* 2019 *Phys. Med. Biol.* **64** 185001

View the [article online](#) for updates and enhancements.

## OPEN ACCESS

## PAPER

RECEIVED  
20 May 2019REVISED  
8 July 2019ACCEPTED FOR PUBLICATION  
25 July 2019PUBLISHED  
11 September 2019

Original content from this work may be used under the terms of the [Creative Commons Attribution 3.0 licence](https://creativecommons.org/licenses/by/4.0/).

Any further distribution of this work must maintain attribution to the author(s) and the title of the work, journal citation and DOI.



# Visualization of gold fiducial markers in the prostate using phase-cycled bSSFP imaging for MRI-only radiotherapy

Yulia Shcherbakova<sup>1,4</sup>, Lambertus W Bartels<sup>1</sup>, Stefano Mandija<sup>2</sup>, Ellis Beld<sup>3</sup>, Peter R Seevinck<sup>1</sup>, Jochem R N van der Voort van Zyp<sup>3</sup>, Linda G W Kerkmeijer<sup>3</sup>, Chrit T W Moonen<sup>1</sup>, Jan J W Legendijk<sup>3</sup> and Cornelis A T van den Berg<sup>3</sup>

<sup>1</sup> Center for Image Sciences, Imaging Division, University Medical Center Utrecht, Heidelberglaan 100, Room Q.03.4.21, 3508 GA Utrecht, The Netherlands

<sup>2</sup> Utrecht University, Utrecht, The Netherlands

<sup>3</sup> Department of Radiotherapy, Imaging Division, University Medical Center Utrecht, Utrecht, The Netherlands

<sup>4</sup> Author to whom any correspondence should be addressed.

E-mail: [Y.Shcherbakova@umcutrecht.nl](mailto:Y.Shcherbakova@umcutrecht.nl)

**Keywords:** MRI-only radiotherapy, bSSFP, MRI, phase-cycled bSSFP, prostate radiotherapy, fiducial marker

## Abstract

In this work, we present a new method for visualization of fiducial markers (FMs) in the prostate for MRI-only radiotherapy with a positive contrast directly at the MR console. The method is based on high bandwidth phase-cycled balanced steady-state free precession (bSSFP) sequence, which is available on many clinical scanners, does not require any additional post-processing or software, and has a higher signal-to-noise (SNR) compared to conventional gradient-echo (GE) imaging. Complex phase-cycled bSSFP data is acquired with different RF phase increment settings such that the manifestation of the artifacts around FMs in the acquired complex images is different for each dynamic acquisition and depends on the RF phase increment used.

First, we performed numerical simulations to investigate the complex-valued phase-cycled bSSFP signal in the presence of a gold FM, and to investigate the relation of the true physical location of the FM with the geometrical manifestation of the artifacts. Next, to validate the simulations, we performed phantoms and *in vivo* studies and compared the experimentally obtained artifacts with those predicted in simulations. The accuracy of the method was assessed by comparing the distances between the FM's centers and the center of mass of FMs system measured using phase-cycled bSSFP MR images and using reference CT (or MRI-only) images.

The results show accurate (within 1 mm) matching of FMs localization between CT and MR images on five patients, proving the feasibility of *in vivo* FMs detection on MR images only. The FMs show a positive contrast with respect to the prostate background on real/imaginary phase-cycled bSSFP images, which was confirmed by simulations.

The proposed method facilitates robust FMs visualization with positive contrast directly at the MR console, allowing RT technicians to obtain immediate feedback on the anticipated feasibility of accurate FMs localization while the patient is being scanned.

## 1. Introduction

External-beam radiotherapy (EBRT) is one of the treatment options for prostate cancer. Fiducial markers (FMs) are used as landmarks for localization of the prostate before the delivery of each radiation fraction (Crook *et al* 1995, Dehnad *et al* 2003, Parker *et al* 2003). For this purpose three or four gold cylindrical FMs (1 mm diameter, 3–5 mm length) are usually implanted in the prostate a couple of weeks before treatment under trans-rectal ultrasound guidance (two markers at the prostatic base on the right and left side and one or two towards the apex of the prostate) (Herman *et al* 2003).

Manual localization of FMs during the treatment planning phase (referred to as simulation phase) is currently done on treatment planning computed tomography (CT) images, considered as the gold standard. FMs

can be localized based on their distinct, local streaking artifacts in CT images, and this procedure is very robust (Nederveen *et al* 2000, Habermehl *et al* 2013, Chan *et al* 2015). Currently, also MR images are being acquired for treatment planning as the soft tissue contrast of MRI offers superior localization of the tumor process. However, such a dual-modality workflow requires two separate imaging sessions, complicating workflow and patient comfort. Also from a more fundamental point of view, a dual imaging modality workflow has a drawback: an extra source of uncertainties is introduced due to a potential registration error between CT and MRI required to fuse the information (Roberson *et al* 2005, Nyholm *et al* 2009).

A potential solution would be to switch to an MRI-only workflow for treatment planning where all information needed in the treatment planning process is acquired solely by MRI (Khoo *et al* 1997, Lee *et al* 2003). A key step towards the clinical feasibility of MRI-only planning has been recent progress to derive electron density information, so-called ‘synthetic CT images’, from MR images (Korhonen *et al* 2014, Kim *et al* 2015, Tyagi *et al* 2017, Maspero *et al* 2017b). Currently, MRI-only planning for radiotherapy treatment of prostate cancer is being performed by several clinics worldwide (Maspero 2018).

A key challenge in the clinical implementation of MRI-only planning of prostate radiotherapy has been the robust and accurate visualization and localization of FMs on MR images. FMs induce magnetic field distortions around them due to the magnetic susceptibility difference between the metallic marker and the tissue surrounding it. These field inhomogeneities cause local artifacts in MR images (Koch *et al* 2010, Hargreaves *et al* 2011), the appearance of which depends on the pulse sequence used and the imaging parameter settings. These artifacts are usually used to determine the position of FMs (Maspero *et al* 2018). As the local magnetic field disturbance caused by the presence of FMs depends on their shape and orientation with respect to the direction of the main magnetic field, so does the visualization of FMs on MR images (Jonsson *et al* 2012).

Gradient-echo (GE) MR imaging is commonly used as a technique for visualization of FMs in the prostate. FMs typically appear as signal voids in GE MR magnitude images, which allows RT technicians to identify and localize them. However, it is difficult to distinguish FMs from other sources of local field inhomogeneities, like hemorrhages and calcifications, which appear as dark spots as well, and thus may resemble FMs (Hong *et al* 2012, Ng *et al* 2014, Chan *et al* 2015, Maspero *et al* 2018).

Recently, an MR-based automatic gold FMs detection method was presented (Maspero *et al* 2017a), which is based on a template matching method applied to the complex MRI data (Zijlstra *et al* 2017). This method utilizes not only the signal voids observed on magnitude images for localization but also phase variations around the markers. Although this facilitates robust automatic localization, the method requires dedicated image processing software which is not readily available at the MR console.

To facilitate successful FM localization, FMs need to be assessed directly at the MR console while a patient is being scanned. This direct feedback allows RT technicians to immediately attempt a new scan or to refer a patient to a regular planning CT exam in case FMs are not present or cannot be directly visualized on the acquired MR images.

In this work, we present a new method for FMs visualization in the prostate for MRI-only radiotherapy, which facilitates FMs visualization with a positive contrast directly at the MR console, allowing RT technicians to immediately and easily localize FMs. The method is based on high bandwidth phase-cycled balanced steady-state free precession (bSSFP) imaging, which has a higher signal-to-noise (SNR) compared to conventional GE imaging (Bieri and Scheffler 2013). Phase-cycled bSSFP is a well-known MR acquisition technique, which is commonly used to eliminate the banding artifacts and to avoid signal loss in the magnitude images, which are caused by sensitivity of bSSFP signal to main magnetic field ( $B_0$ ) inhomogeneities (Zur *et al* 1990, Bangerter *et al* 2004, Lauzon and Frayne 2009, Brown *et al* 2014). Phase-cycled bSSFP is a dynamic sequence with a predetermined number of dynamic acquisitions, in which the RF phase is linearly increased from one dynamic to another, which shifts the off-resonance profile of the signal dependently on the RF phase increment. The contrast of FMs in the phase-cycled bSSFP images varies between each dynamic acquisition because the manifestations of the susceptibility artifacts around FMs on MR images depend on the RF phase increment.

To be able to optimize the method, we performed simulations to investigate the complex-valued phase-cycled bSSFP MR signal in the presence of one gold FM, and to investigate the relation of the true physical location of the FM with the geometrical manifestation of the artifacts. To validate the simulations, we performed phantoms and *in vivo* studies and compared the obtained experimentally artifacts with those predicted in simulations. The accuracy of the method was assessed in a phantom and *in vivo* by comparing the distances between the FM’s centers and the center of mass of FMs system measured using MR images acquired with the proposed phase-cycled bSSFP method and using CT (or MRI-only) images acquired with the reference techniques.

## 2. Methods

### 2.1. Phase-cycled bSSFP signal model

RF phase cycled bSSFP is a dynamic scan, where for each dynamic acquisition the phase of the RF excitation pulse is increased stepwise from one dynamic to another according to a certain RF phase incrementing scheme. For

each dynamic acquisition the complex transverse magnetization  $M_{xy}$  can be described as (Lauzon and Frayne 2009, Xiang and Hoff 2014, Shcherbakova *et al* 2018):

$$M_{xy} = M_{\text{eff}} \cdot \frac{1 - ae^{i\theta}}{1 - b \cos \theta} \cdot e^{i\varphi}, \quad (1)$$

where  $M_{\text{eff}}$ ,  $a$ ,  $b$  are the parameters dependent on the repetition time TR, the echo time TE, the relaxation times  $T_1$  and  $T_2$ , the flip angle  $\alpha$ , see equations (1)–(3) in (Shcherbakova *et al* 2019).  $\theta$  is the resonance offset angle (in radians),  $\theta = \theta_0 - \Delta\theta$ , where  $\theta_0 = 2\pi (\delta_{\text{CS}} + \gamma\Delta B_0) TR$ ,  $\gamma\Delta B_0$  is the spatially varying off-resonance (in Hz), which includes the background term  $\gamma\Delta B_{0\text{background}}$  and the term related to the presence of the FM  $\gamma\Delta B_{0\text{FM}}$ ,  $\gamma\Delta B_0 = \gamma\Delta B_{0\text{background}} + \gamma\Delta B_{0\text{FM}}$ , both terms are spatially dependent although  $\gamma\Delta B_{0\text{FM}}$  is strongly spatially localized around the FM.  $\delta_{\text{CS}}$  is the chemical shift of the species (in Hz) with respect to the water peak,  $\Delta\theta$  is the phase increment (in radians) of the RF excitation pulse,  $\varphi = 2\pi (\delta_{\text{CS}} + \gamma\Delta B_0) TE + \varphi_{\text{RF offset}}$ ,  $\varphi_{\text{RF offset}}$  is the RF phase offset, related to the combination of RF transmit and receive phases (in radians). The use of phase-cycling shifts the off-resonance profile of the signal dependently on the RF phase increment, which is usually set to  $\Delta\theta = \frac{2\pi n}{N}$  (Bangerter *et al* 2004), where  $n$  is the number of  $n$ th dynamic acquisition,  $N$  is the total number of dynamic acquisitions.

The RF phase offset  $\varphi_{\text{RF offset}}$  and the chemical shift of the species  $\delta_{\text{CS}}$  are constant offsets. Without loss of generality, we chose them to be zero.

## 2.2. Simulations

Simulations of the phase-cycled bSSFP signal in the presence of one cylindrical gold FM (1 mm diameter, 5 mm length) were performed. Simulations were adopted from the work by Beld *et al* (2019), where the bSSFP steady-state signal in equation (1) was assumed to be proportional to the effective spin density distribution. The complex-valued 3D phase-cycled bSSFP MR signal was simulated for two cases:  $\gamma\Delta B_{0\text{background}} = 0$  and  $\gamma\Delta B_{0\text{background}} = -15$  Hz. The RF phase incrementing scheme  $\Delta\theta = [0, \frac{\pi}{3}, \frac{2\pi}{3}, \pi, \frac{4\pi}{3}, \frac{5\pi}{3}]$  was used.

The scan parameter settings in the simulations were the same as the protocol parameter settings of the MR sequence used for the experiment on the phantom with one FM: field strength 3T, TE = 3.3 ms, TR = 6.7 ms, FA = 25°, FOV = 50 × 50 × 50 mm<sup>3</sup>, readout bandwidth = 905.8 Hz, readout direction LR, 6 dynamic acquisitions with increment  $\Delta\theta = \pi/3$ , voxel size 1 × 1 × 1 mm<sup>3</sup>, susceptibility of gold  $\chi_{\text{Au}} = -34$  ppm, susceptibility of water  $\chi_{\text{water}} = -9.05$  ppm. 10 × 10 × 10 = 10<sup>3</sup> isochromats were simulated per voxel for an image with 1 × 1 mm<sup>2</sup> in-plane voxels and a slice thickness of 1 mm. The relaxation times for the prostate at 3T were used for the simulations of the signal arising from the background tissue, with  $T_1 = 1400$  ms,  $T_2 = 80$  ms (Bojorquez *et al* 2017).

All simulations and calculations were performed in MATLAB R2015a (The MathWorks Inc, Natick, United States).

## 2.3. Experiments

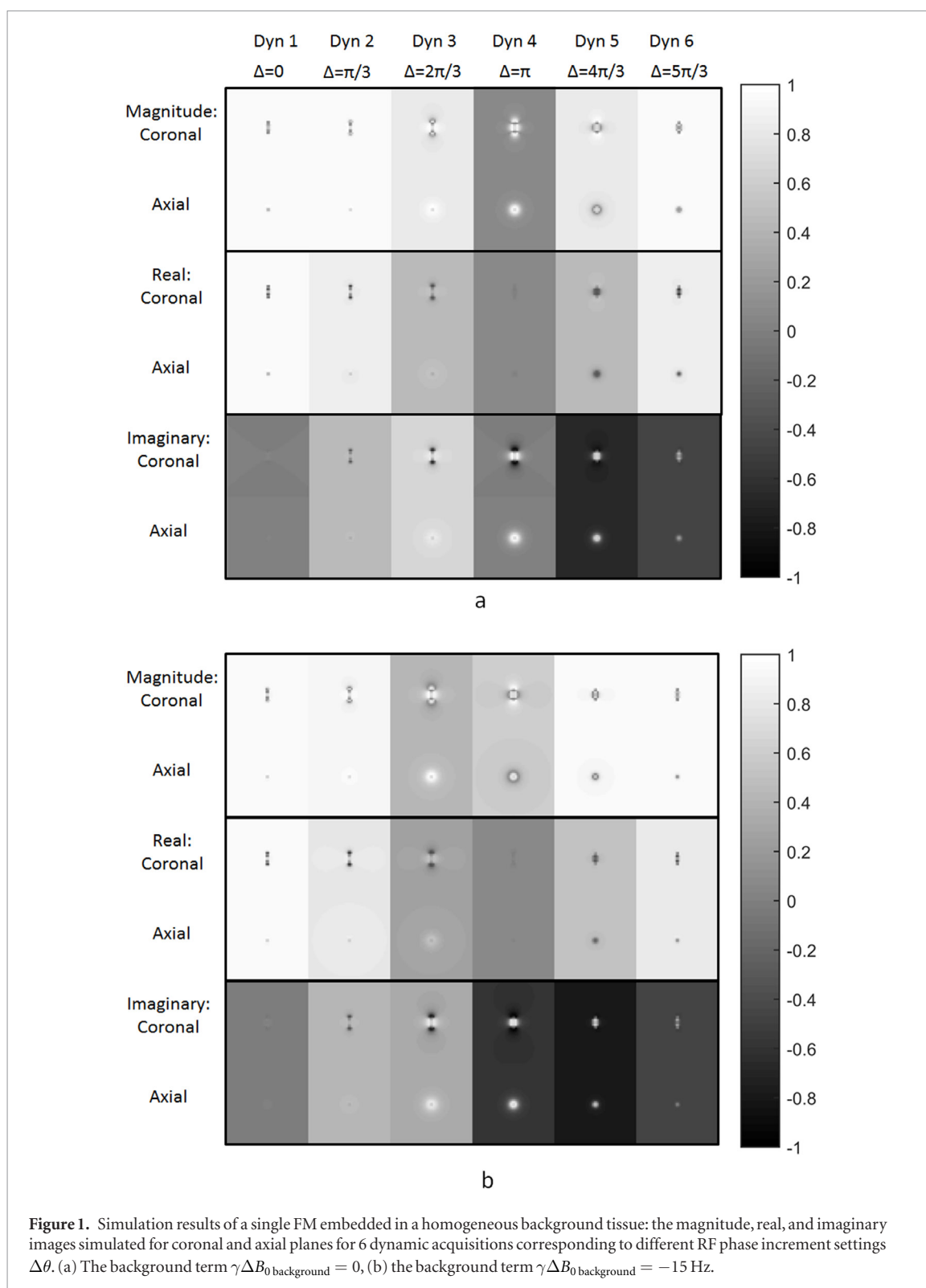
### 2.3.1. Phantom

First, to validate the simulations, we compared the artifact patterns obtained in a phantom experimentally with those predicted by simulations. The experiment was performed using a clinical 3T MR scanner (Philips Ingenia, Best, The Netherlands) on an agar gel phantom with one gold FM (GM1054) implanted. A 15-channel head receive coil was used. Complex 3D phase-cycled bSSFP data were acquired using the following protocol parameter settings: TR 6.7 ms, TE 3.3 ms, FA 25°, FOV 200 × 200 × 60 mm<sup>3</sup>, acquisition voxel size 1 × 1 × 1 mm<sup>3</sup>, reconstruction voxel size 0.89 × 0.89 × 1 mm<sup>3</sup>, 6 dynamic acquisitions with RF phase increment  $\Delta\theta = [0, \frac{\pi}{3}, \frac{2\pi}{3}, \pi, \frac{4\pi}{3}, \frac{5\pi}{3}]$ , scan time 03:59 min.

In spoiled gradient echo (SPGR) imaging, the echo time TE is the most important parameter related to the susceptibility artifact's size. In bSSFP imaging, the echo time TE is always equal to TR/2. To investigate, how the choice of TR influences the FM's visualization in bSSFP images, complex 3D phase-cycled bSSFP data were additionally acquired for two different TR settings: TR = 4.9 ms and TR = 10 ms. The results were compared with the case of TR = 6.7 ms. FA = 25°. Note that TE = TR/2 for each case.

Next, to assess the accuracy of the FMs localization, the experiment was performed on an agar gel phantom with four gold FMs (GM1054) implanted using the same MR scanner with the same coil. Complex 3D phase-cycled bSSFP data were acquired using the following protocol parameter settings: TR 6.7 ms, TE 3.3 ms, FA 25°, FOV 320 × 320 × 60 mm<sup>3</sup>, acquisition voxel size 1.5 × 1.5 × 2 mm<sup>3</sup>, reconstruction voxel size 1 × 1 × 1 mm<sup>3</sup>, 6 dynamic acquisitions with  $\Delta\theta = [0, \frac{\pi}{3}, \frac{2\pi}{3}, \pi, \frac{4\pi}{3}, \frac{5\pi}{3}]$ , scan time 02:07 min. A CT scan of the same phantom was acquired using a Philips Brilliance CT Big Bore (Philips, Best, The Netherlands) with the following parameter settings: 120 kVp, exposure 450 mAs, FOV 369 × 369 × 200 mm<sup>3</sup>, voxel size 0.72 × 0.72 × 1 mm<sup>3</sup>.

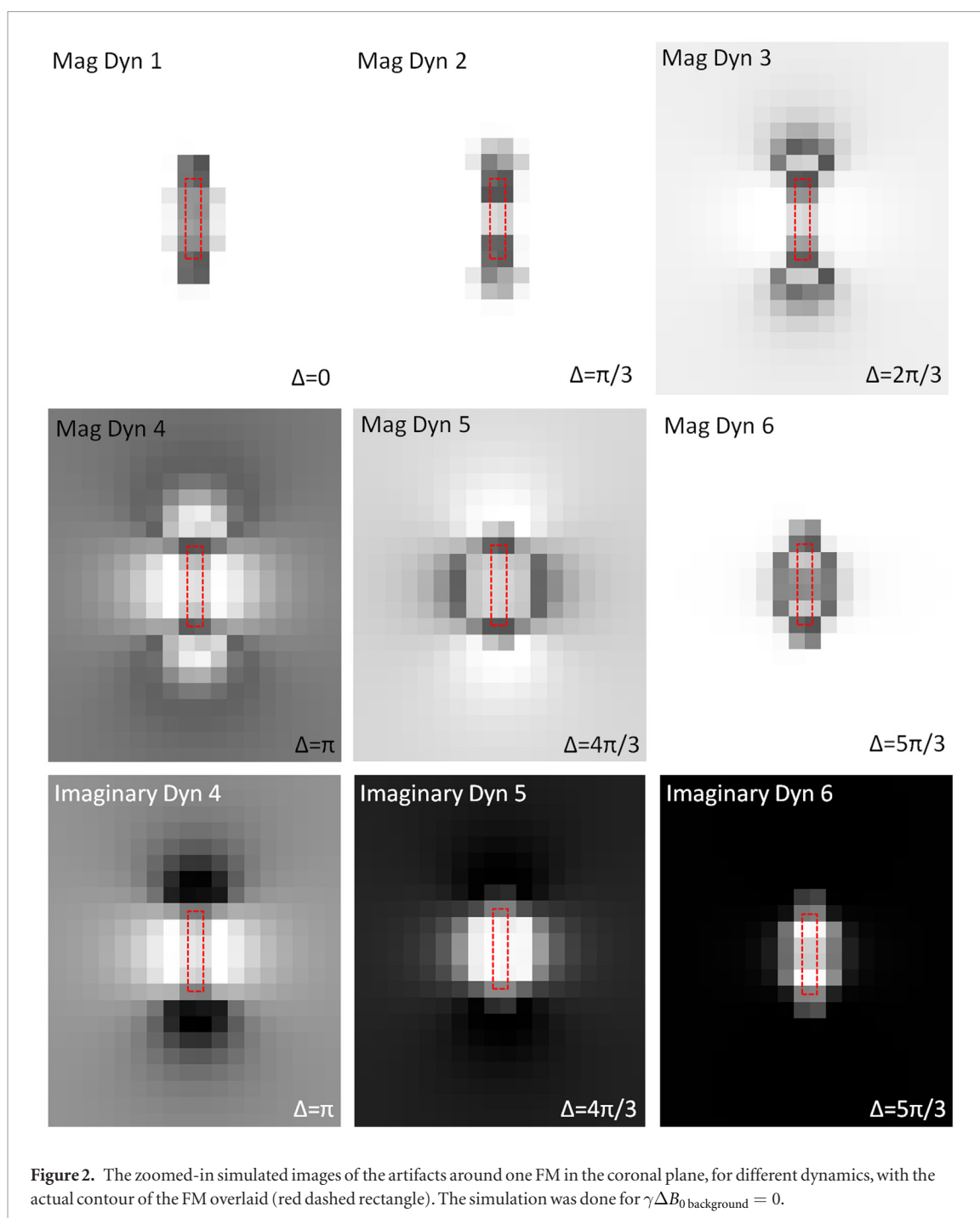
The coordinates of the top and the bottom of each FM were measured both on MR and CT images by a single observer using an in-house developed tool called Volumetool (Bol *et al* 2009). Using the measured coordinates,



the coordinates of the centers on FMs were calculated. Next, the coordinates of the center of mass (average coordinates) were calculated, and the distances from FM's centers to the center of mass were calculated. The accuracy of detecting FMs was assessed by comparing the calculated distances using MR and CT images.

### 2.3.2. *In vivo*

Ten patients participated in this study: five patients were scanned according to our institution's standard clinical EBRT protocol which includes MRI and CT exams. The other five patients were scanned according to the clinical MRI-only protocol. Patient data was acquired in accordance with regulations set out by the local institutional review board. For all ten patients, in addition to clinical MRI EBRT protocol, complex 3D phase-cycled bSSFP data were acquired on a clinical 3T MR scanner using a 16-channel anterior receive coil combined with the



posterior receive coil integrated into the MR table. The protocol parameter settings were used: TR 6.7 ms, TE 3.3 ms, FA 25°, FOV 320 × 320 × 60 mm<sup>3</sup>, acquisition voxel size 1.5 × 1.5 × 2 mm<sup>3</sup>, reconstruction voxel size 1 × 1 × 1 mm<sup>3</sup>. Water-selective binomial excitation (ProSet type 1-3-3-1) was used for fat suppression. The acquisition time was 02:07 min. For all ten patients, the coordinates of the top and the bottom of each FM were identified on the acquired phase-cycled bSSFP MR images by a single observer using Volumetool. Next, the coordinates of the centers of FMs and the center of mass were calculated, as well as the distances from FM's centers to the center of mass (as was done for the phantom).

CT scans of 5 out of 10 patients were acquired according to our clinical CT EBRT protocol on a Philips Brilliance CT Big Bore scanner, with the following parameter settings: 120 kVp, exposure range for five patients was (83–186) mAs, FOV 446 × 446 × 279 mm<sup>3</sup>, voxel size 0.87 × 0.87 × 3 mm<sup>3</sup>. For these 5 patients, the coordinates of the top and the bottom of each FM were identified on CT images by a single observer using Volumetool. Next, the coordinates of the centers of FMs and the center of mass were calculated as well as the distances from FM's centers to the center of mass. The accuracy of the localization of FMs was assessed by comparing the calculated distances using MR and CT images.

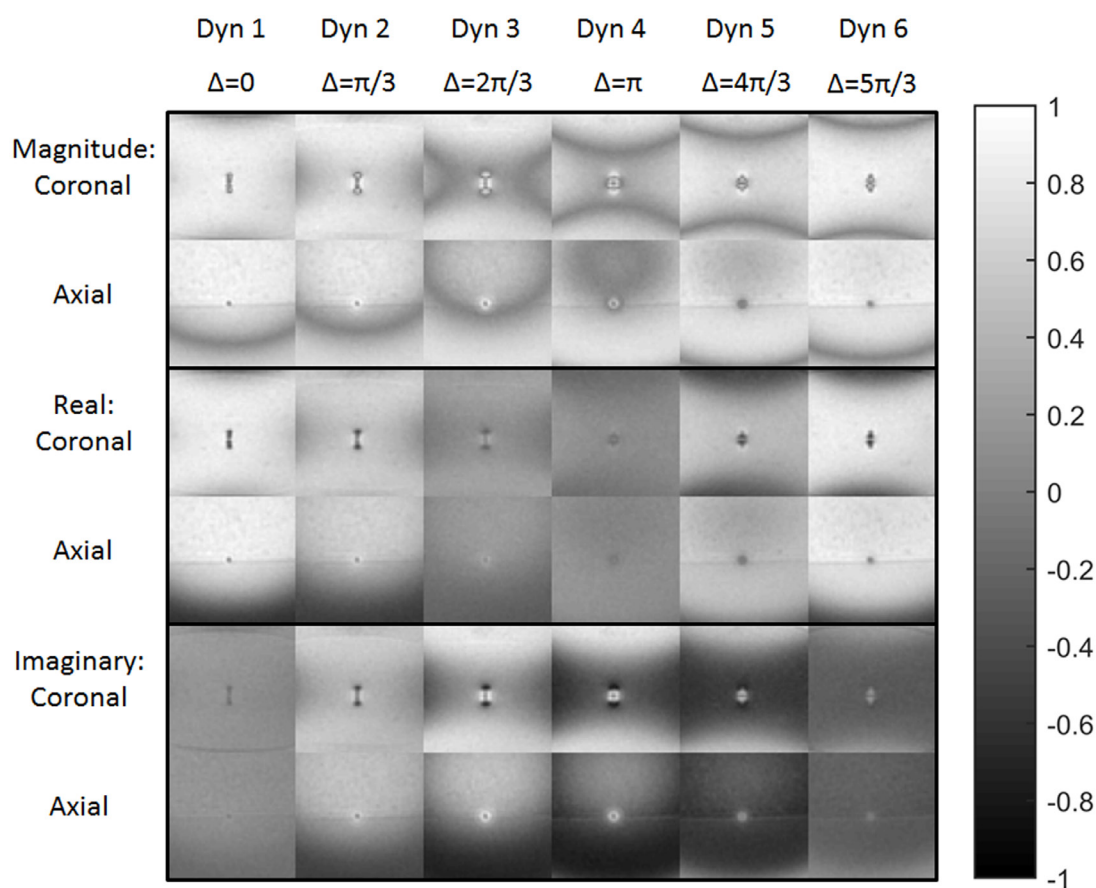


Figure 3. Experimental results of the phantom with one gold FM implanted: the magnitude, real, and imaginary images for coronal and axial planes for six dynamic acquisitions corresponding to different RF phase increment settings. The data was acquired in 3D and shown only for 2 middle orthogonal slices.

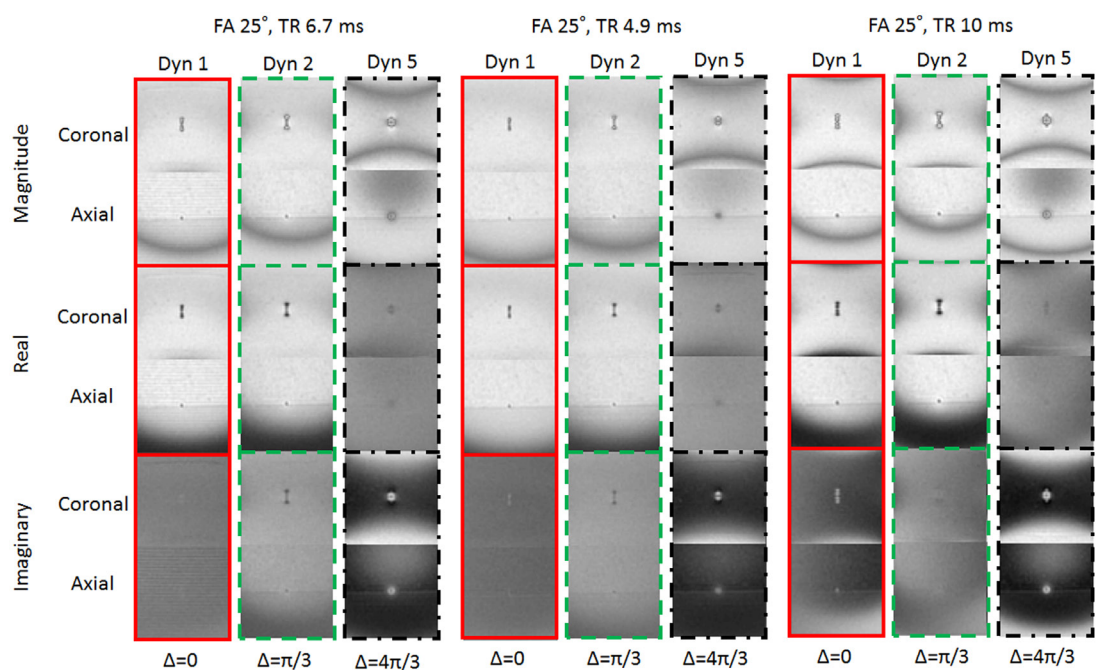
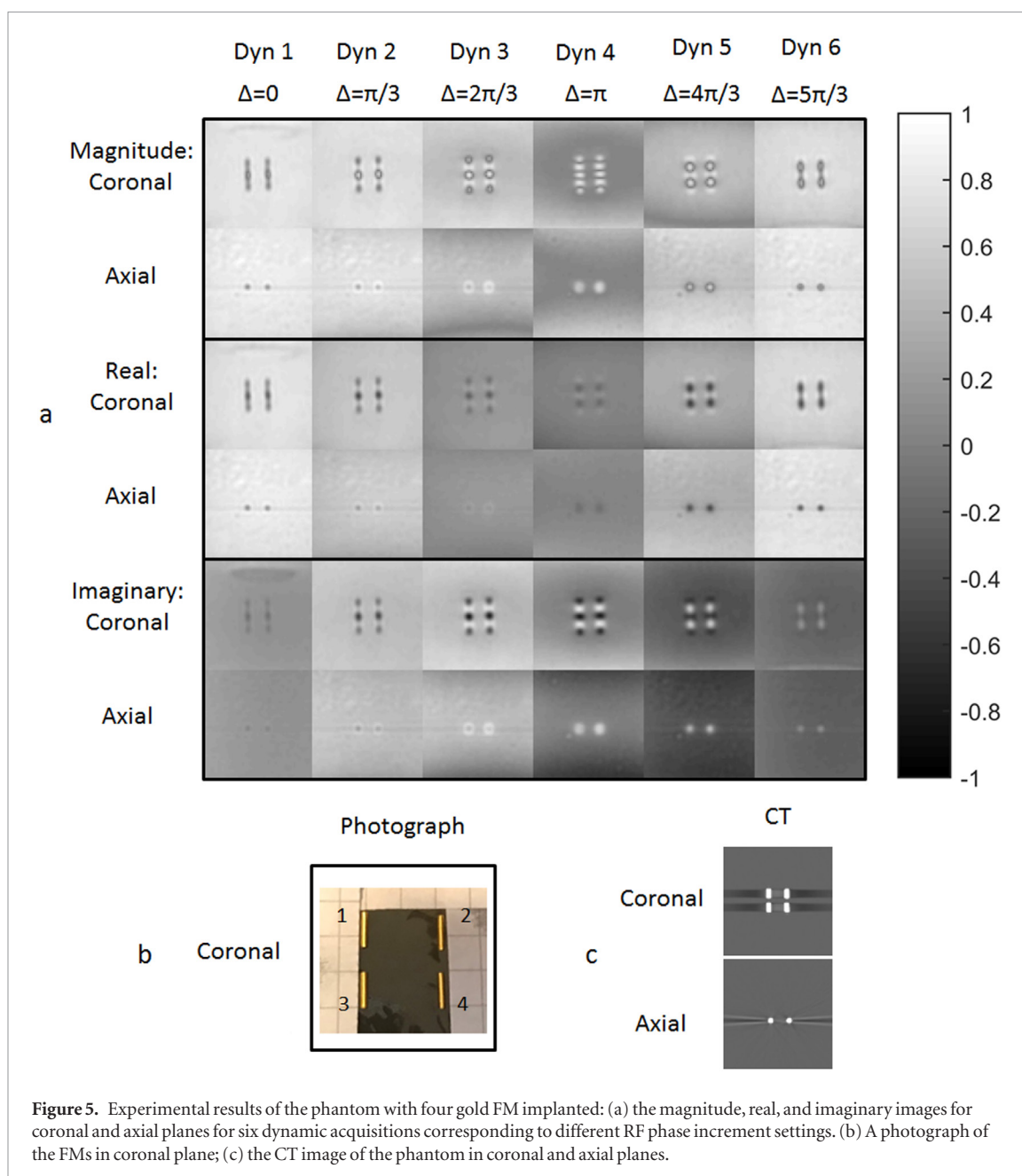
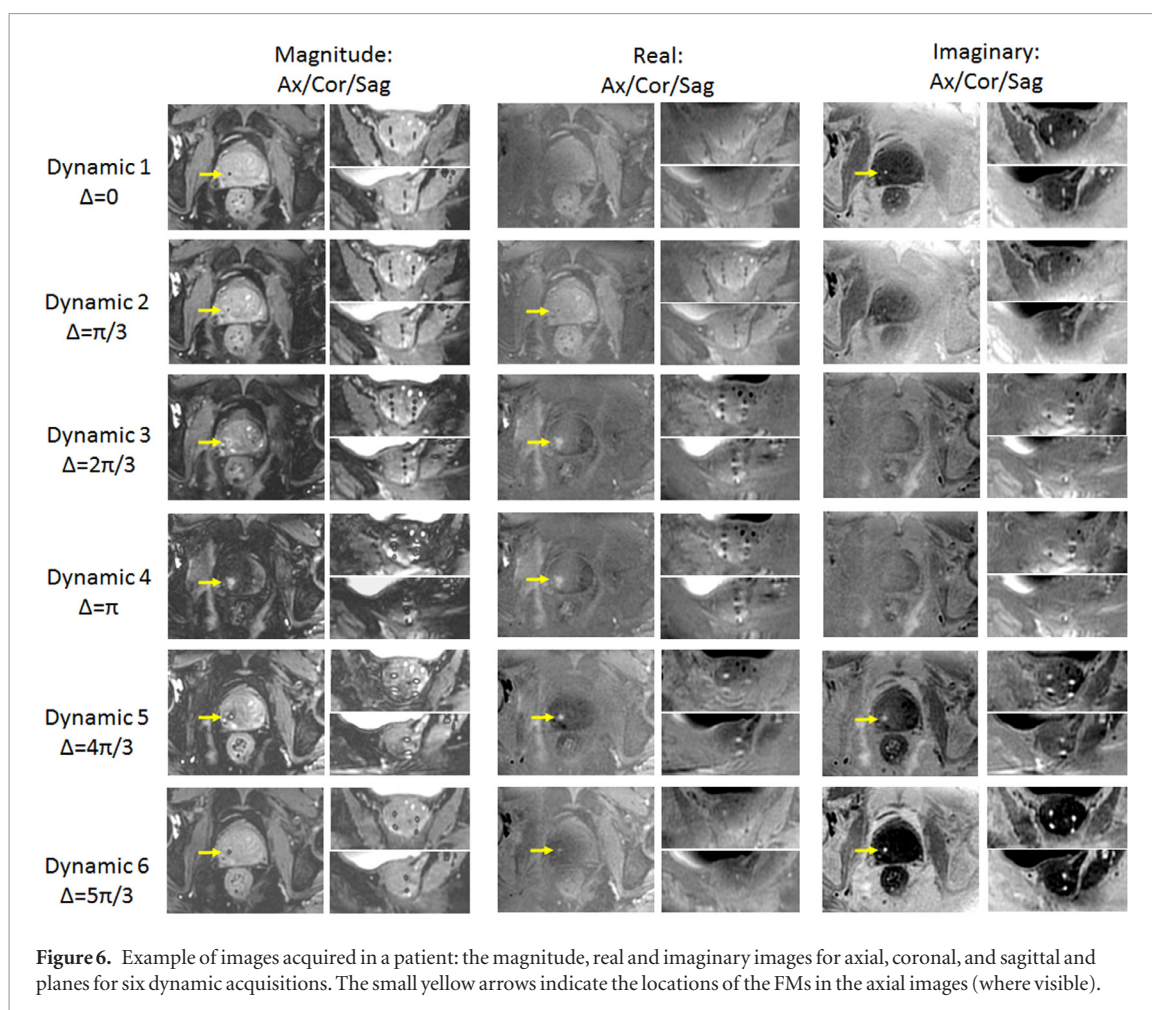


Figure 4. Comparison of the images acquired with different TR settings: the magnitude, real, and imaginary images for coronal and axial planes for dynamics number 1 (red solid frame), number 2 (green dashed frame), and number 5 (black dash dotted frame). Corresponding RF phase increment settings are  $\Delta = 0, \pi/3, 4\pi/3$ . Three cases are shown: TR = 6,7 ms, TR = 4,9 ms, TR = 10 ms. FA = 25° and TE = TR/2 for each case.

**Table 1.** The measurements in the phantom with four FMs implanted.

Type of imaging	Distance ( $D_n$ ) between the center of the $n$ th FM and the center of mass of FMs system (mm)			
	$D_1$	$D_2$	$D_3$	$D_4$
CT	7.0	7.0	6.9	7.0
MRI	7.0	7.1	7.0	7.1
Deviation(MRI-CT)	0	0.1	0.1	0.1

For the other five patients, which were scanned under clinical MRI-only protocol and thus no CT images were available, the coordinates of top and bottom of FMs were identified using MR images acquired with a clinically used high resolution bSSFP SPAIR (Spectral Attenuated Inversion Recovery) sequence in our radiotherapy department's MRI-only protocol (FOV  $250 \times 250 \times 90 \text{ mm}^3$ , acquisition voxel size  $1 \times 1 \times 2 \text{ mm}^3$ , reconstruction voxel size  $0.49 \times 0.49 \times 1 \text{ mm}^3$ ). The acquisition time was 02:07 min. The coordinates of the centers of FMs and the distances from the FM's centers to the center of mass were calculated. The accuracy of detecting FMs was assessed by comparing the calculated distances using both types of MR images.



Next, we visually compared the acquired dynamic images for all ten patients and investigated which dynamic, i.e. which RF phase increment, allows for the best visualization of FMs. As a result, a certain dynamic was selected, and the coordinates of the centers of FMs were identified using the selected scan. Again, the distances from FM's centers to the center of mass of the FM's system were calculated. The accuracy of detecting FMs, in this case, was assessed by comparing the calculated distances using MR images acquired with the proposed phase-cycled bSSFP method with the reference measurements (CT or MR SPAIR bSSFP for MRI-only), and the corresponding Bland-Altman plots were made.

### 3. Results

#### 3.1. Simulations

Simulation results for one gold FM are shown in figure 1. Magnitude, real and imaginary images are shown for coronal and axial planes for six dynamic acquisitions corresponding to different RF phase increments for two different spatially constant  $\gamma\Delta B_{0\text{background}}$  values: 0 Hz and  $-15$  Hz. A distinct artifact pattern can be seen in all simulated dynamic images for both values of  $\gamma\Delta B_{0\text{background}}$ . A shift of about one dynamic in the artifact pattern can be observed between these cases, which is caused by the difference in  $\gamma\Delta B_{0\text{background}}$ . Figure 2 shows the zoomed-in images of the FM in the coronal plane, with the actual contours of the FM overlaid (case  $\gamma\Delta B_{0\text{background}} = 0$ ). The artifacts exceed the actual size of the FM as expected since the field disturbances extend beyond the FM.

Both ends (top and bottom) of the FM are especially well visible on the images of dynamics number 1 (RF phase increment  $\Delta\theta = 0$ ) and number 2 (RF phase increment  $\Delta\theta = \pi/3$ ). Interestingly, on the imaginary image of dynamics number 5 (RF phase increment  $\Delta\theta = 4\pi/3$ ) and number 6 (RF phase increment  $\Delta\theta = 5\pi/3$ ), the center of the bright spot on a dark background corresponds to the center of the FM, as can be seen in figure 2.

The simulations show that signal localization corresponds with the physical locations of the FM.

#### 3.2. Experiments in the phantoms

MR images acquired in the phantom with one FM are shown in figure 3. Magnitude, real, and imaginary images are shown for six dynamic acquisitions for coronal and axial planes. The experimental  $\gamma\Delta B_{0\text{background}}$

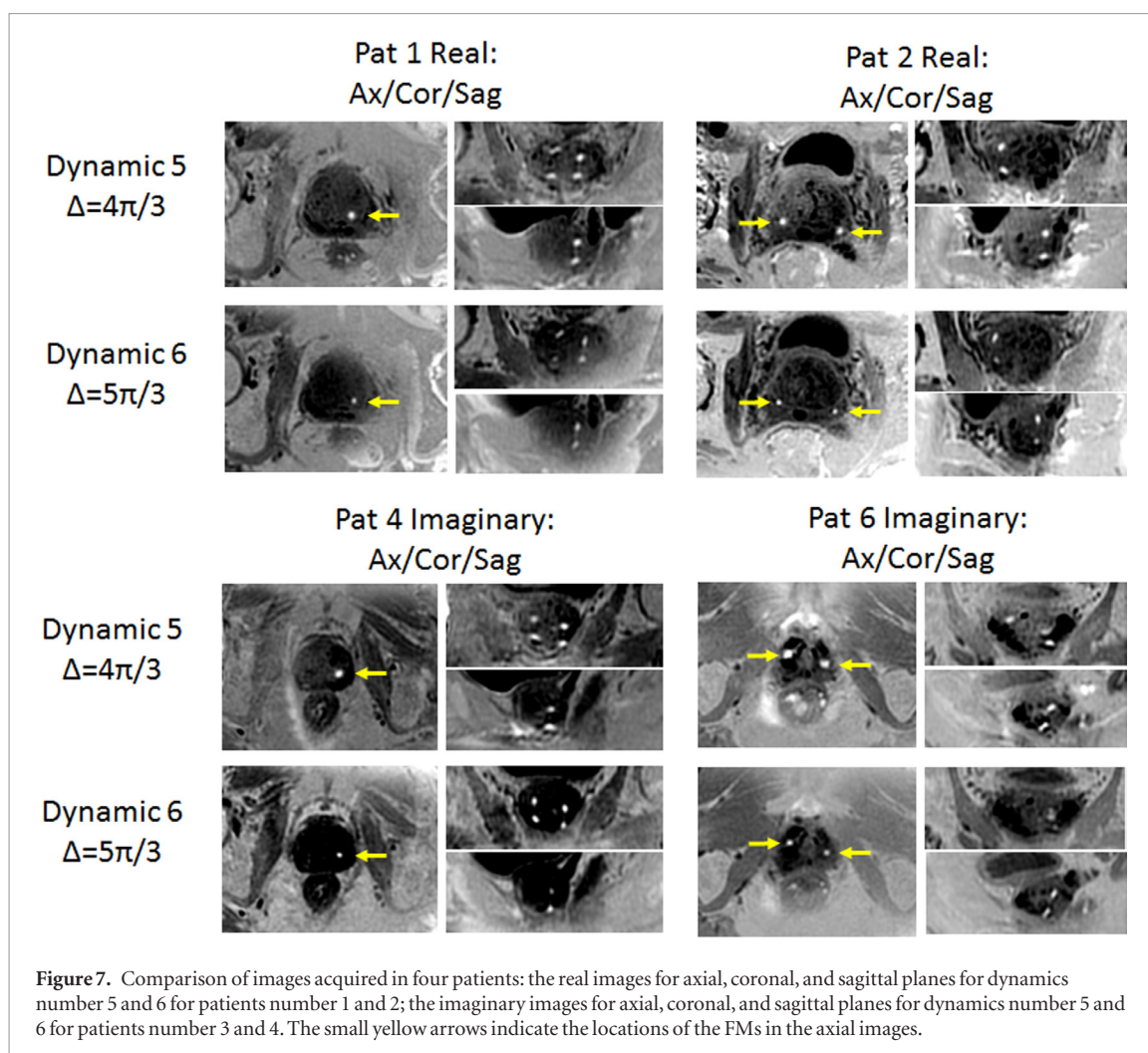


**Figure 7.** Comparison of images acquired in four patients: the real images for axial, coronal, and sagittal planes for dynamics number 5 and 6 for patients number 1 and 2; the imaginary images for axial, coronal, and sagittal planes for dynamics number 5 and 6 for patients number 3 and 4. The small yellow arrows indicate the locations of the FMs in the axial images.

was found to be approximately  $-15$  Hz in the center of the FM (by interpolating the background field not disturbed by FMs). The results match the simulation results shown in figure 1(b). The images show a distinct MR contrast between the FM and the background for each dynamic. Unlike in the simulated MR images, where the background tissue signal is homogeneous, dark bands can be observed in MR images acquired in the phantom. These bands are known as banding artifacts and they are caused by the abrupt loss of the bSSFP signal at particular off-resonances. The spatially varying background  $B_0$  field in the phantom was not included in the simulations, where it was assumed spatially constant. In all the images in the axial plane a line can be observed in the middle of the phantom. This effect is related to the way the phantom was built: the second layer of agar was placed on the first layer containing the FM.

A comparison of the images acquired with different TR settings is presented in figure 4. The magnitude, real, and imaginary images are shown in coronal and axial planes for three dynamics number 1, number 2, and number 5. Only very small differences can be observed in the FM's artifacts. The contrast differences are caused by different signal intensities acquired at different TR settings. The banding artifacts appear differently since their locations depend on TR as well. The echo time TE (which is equal to  $TR/2$ ) almost does not change the appearance of the artifacts.

The experimental results of scanning the phantom with four FMs are shown in figure 5. Magnitude, real, and imaginary images are shown for 6 dynamic acquisitions for coronal and axial planes through the 3D volume. The same distinct artifact pattern, which was predicted in simulations and which was seen in the experimental results in the phantom with one FM, can be observed here as well. The only difference here is that there are four FMs placed close to each other causing the artifact pattern to be slightly different. A photograph of the coronal plane and corresponding CT images for coronal and axial planes are shown for comparison. The distances between the FM's centers and the center of mass measured using MR and CT images are provided in table 1.

### 3.3. Experiments *in vivo*

The acquired data for ten patients were processed. An example of MR images of the prostate of a patient with four implanted FMs is shown in figure 6. A similar varying contrast pattern (dependent on the RF phase increment

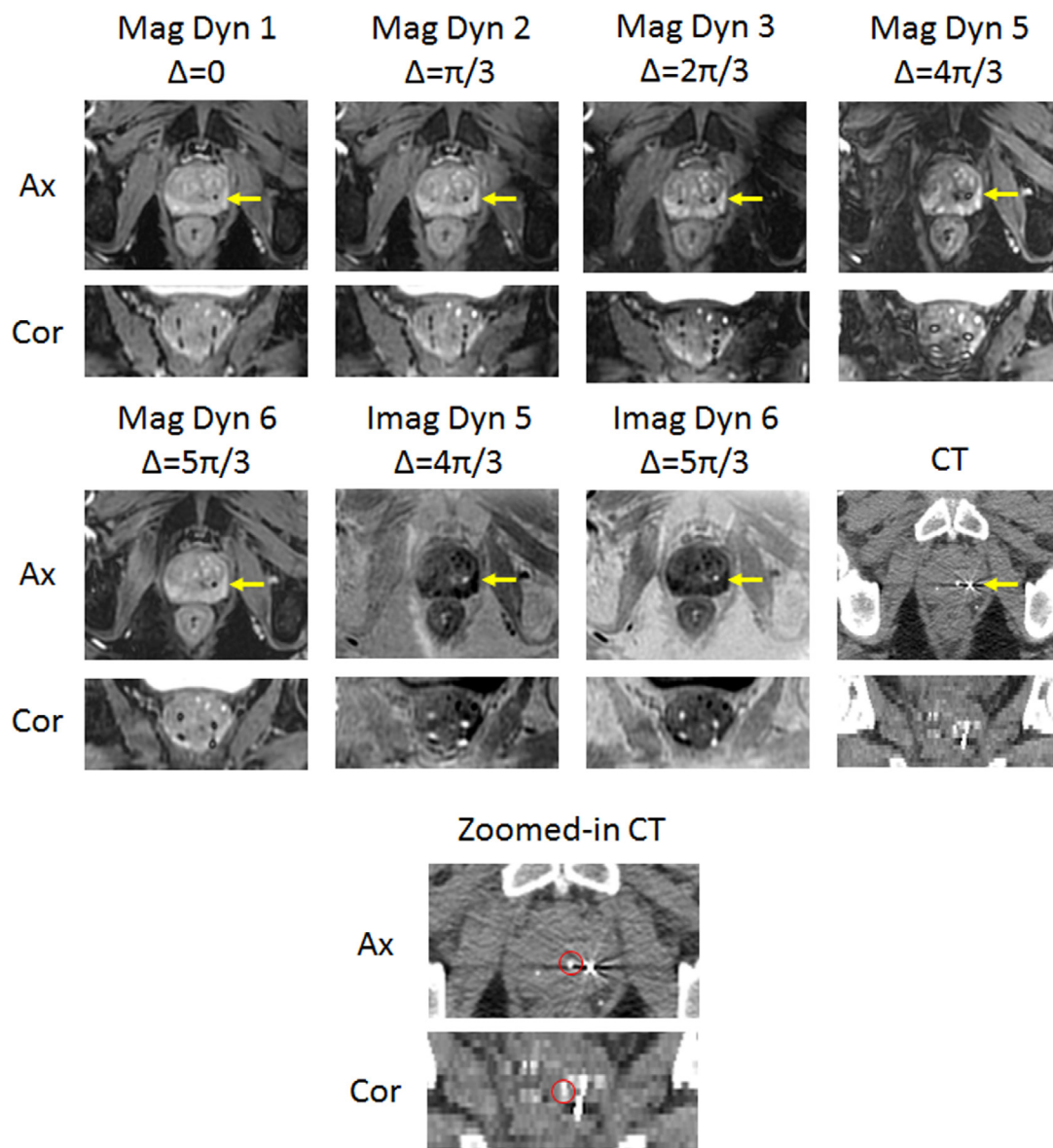
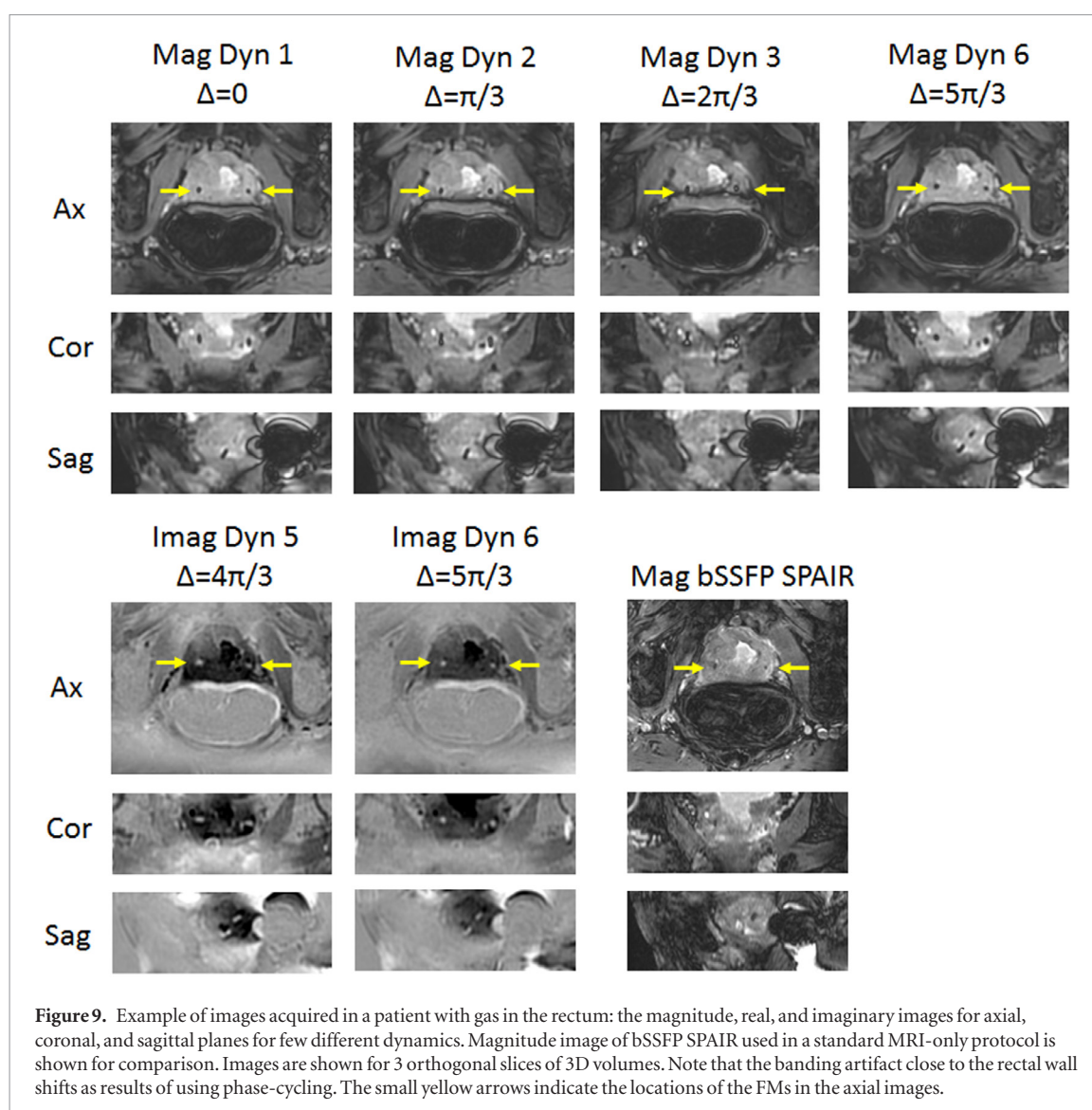


**Figure 8.** Example of images acquired in a patient with calcification in the prostate (identified with CT): the magnitude, real, and imaginary images for axial and coronal planes for few different dynamics; the CT images for axial and coronal planes. The small yellow arrows indicate the locations of the one of the FMs in the axial images. The calcification is marked with red circle on zoomed-in CT images.

used) as induced by FM in the phantom, can be seen in this patient. FMs can be distinctly seen in the acquired images and they show distinct artifact pattern. FMs appear very bright on the imaginary images of dynamics number 5 (RF phase increment  $\Delta\theta = 4\pi/3$ ) and number 6 (RF phase increment  $\Delta\theta = 5\pi/3$ ). This positive contrast facilitates a relatively straight forward direct visual localization of the FMs by an observer. Similar results were obtained in the other nine patients: the bright appearance of the FMs was observed on dynamics number 5 and 6 of real or imaginary images dependent on the actual RF phase offset  $\varphi_{RF \text{ of fset}}$  (which was assumed to be zero in simulations). The results for 4 patients are shown in figure 7. Since the center of the FM is the center of the bright spot, as shown in figure 2, imaginary/real images of dynamics number 5 and number 6 can be used directly for localization of the FM's centers.

An example of a patient with calcification in the prostate is shown in figure 8. FMs show distinct behavior in all acquired images as expected. Calcification was observed at CT images as a bright spot without streaking artifacts. At MR images the same calcification was observed as a dark spot on the magnitude images and a slightly bright spot on a dark prostate background on the imaginary images. We did not observe any significant changes in the appearance of this calcification in MR images for different RF phase increments.

An example of the performance of the method in a patient with rectal gas is shown in figure 9. The banding artifacts, which can be seen on the prostate area, are caused by rectal gas, and their position depends on the RF phase increment. However, the FMs can still be clearly visualized over all dynamics, and the artifact pattern



remains similar to the one predicted by simulations and obtained experimentally in other patients. The use of phase-cycling shifts the spatial location of the banding artifacts. Thus, there will always a phase-cycled image, where the bands do not coincide with the FMs.

### 3.4. Accuracy of the FMs localization

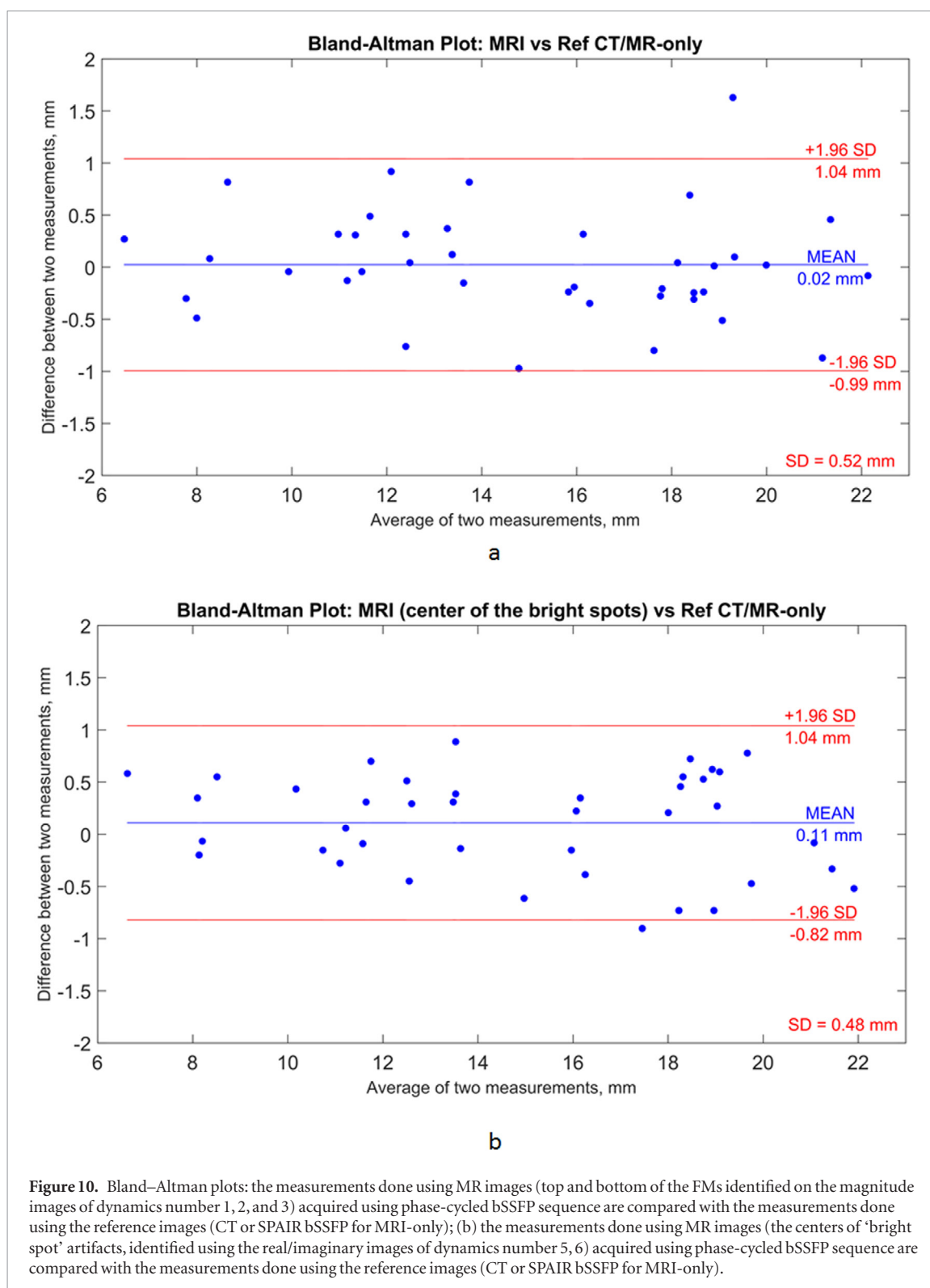
In the phantom, the differences in distances measured between the centers of the FMs and the center of mass on MR and CT images using Volumetool are shown in table 1. The errors are within 0.2 mm.

*In vivo* results are presented in figure 10: Bland–Altman plots comparing two measurement methods are shown: (a) the measurements done using the phase-cycled bSSFP MR images (top and bottom of FMs identified on the magnitude images of dynamics number 1, 2, and 3) are compared with the measurements done using the reference images (CT or SPAIR bSSFP for MRI-only); (b) the measurements done using the phase-cycled bSSFP MR images (the centers of ‘bright spot’ artifacts, identified using the real/imaginary images of dynamics number 5, 6) are compared with the measurements done using the reference images (CT or SPAIR bSSFP for MRI-only).

In these plots, the differences between the two methods are plotted against the averages of these two methods. Horizontal lines are drawn at the mean difference and at the limits of agreement, which were defined as the mean difference plus and minus 1.96 times the standard deviation of the differences. The mean values for both cases are close to zero. Standard deviations were around 0.5 mm.

## 4. Discussion

In this work, we introduced a new method for FMs visualization in the prostate with positive contrast for MRI-only radiotherapy, which is based on the phase-cycled bSSFP sequence. There are other techniques for visualization of markers with positive contrast (Seppenwoolde *et al* 2003, Mani *et al* 2006, Seevinck *et al* 2011,



Dong *et al* 2015), however, they rely on non-standard acquisition modifications or dedicated post-processing software. We opted for the use of bSSFP sequence for this purpose, since it is available on most clinical scanners, works without the need for dedicated post-processing software, provides the highest SNR efficiency with respect to other existing MR sequences, and allows for good visualization of the prostate. The bSSFP sequence employs a relatively short TR, leading to acceptable acquisition time and high bandwidth, ensuring geometric fidelity.

The presented method is based on acquiring complex phase-cycled bSSFP data with different RF phase increment settings such that the manifestation of the artifacts around FMs in the acquired complex images is different for each dynamic acquisition and depends on the RF phase increment used.

By inspecting the acquired dynamic complex images, a certain dynamic can be chosen and used by RT technicians for FMs localization. We found that the imaginary/real images of dynamics number 5 and number 6 pro-

vide optimal positive contrast for direct localization of the FM's centers (applicable at 3T, TR 6.7 ms, TE 3.3 ms, six dynamics with RF phase increment  $\Delta\theta = [0, \frac{\pi}{3}, \frac{2\pi}{3}, \pi, \frac{4\pi}{3}, \frac{5\pi}{3}]$ ). The simulations and phantom results indicate that the centers of bright spots within a dark prostate background coincide with the FM's centers. Hence, the proposed method facilitates FMs visualization with a positive contrast directly at the MR console, allowing RT technicians to localize FMs during the scan session.

However, a bright appearance of the FMs on real or imaginary images of dynamics number 5 and number 6 depends on the actual background  $B_0$  field. Spatial variations of the  $B_0$  field induce differences in the artifacts around FMs in MR images. As we showed in the simulations, different background  $B_0$  field causes a shift in the artifact pattern. In the prostate, the  $B_0$  field is usually quite homogeneous with the differences in  $\gamma\Delta B_{0\text{background}}$  in the range  $[-10\text{ Hz}; 10\text{ Hz}]$  or maximum absolute differences in  $\gamma\Delta B_{0\text{background}}$  within the prostate of around 20 Hz. Due to imperfect shimming or  $B_0$  drift, the off-resonance  $\gamma\Delta B_{0\text{background}}$  can vary even more, in such a case the bright appearance of the FMs can be observed on different dynamics, shifted relative to the original one, for example, number 4 and number 5, or number 6 and number 1.

In general, for a similar experimental setup (field strength 3T, TR 6.7 ms, TE 3.3 ms, 6 dynamics with RF phase increment  $\Delta\theta = [0, \frac{\pi}{3}, \frac{2\pi}{3}, \pi, \frac{4\pi}{3}, \frac{5\pi}{3}]$ , we believe that for most patients with the same gold FMs, the positive contrast will be visible in dynamics number 5 ( $\Delta\theta = \frac{4\pi}{3}$ ) and number 6 ( $\Delta\theta = \frac{5\pi}{3}$ ). At different magnetic field strengths and/or different MR acquisition parameter settings, the appearance of FMs might be different, and the RF phase increment for which positive contrast is seen may vary. Nevertheless, FMs will always show positive contrast with the background at certain specific RF phase increment.

The simulations were performed for a single FM. In reality four FMs will be implanted in the prostate, however, we do not expect them to influence each other's appearance. The changes in the local magnetic field due to the presence of a neighboring FM are very small compared to the local magnetic field. Therefore, the magnetic moment of a FM will not be affected by the magnetic moment of others FMs.

The simulations were only performed when a FM was parallel to the main magnetic field. We observed similar artifact patterns in cases with slight angulations of FMs, which occurred in some patients. We did not see any significant artifact deviations in all ten patients included in this study.

In 1 out of 10 patients we observed calcification. FMs, in this case, showed a distinct behavior in all acquired dynamic images, whereas calcification remained almost the same in all acquired images. We expect that calcification cannot replicate the FM's artifact pattern and therefore they can be distinguished from one another.

The main drawback of using bSSFP imaging is the presence of banding artifacts on the acquired magnitude images due to  $B_0$  inhomogeneity. The use of shorter TR might help to shift the banding artifacts towards outer FOV.  $B_0$  distortions are often caused by the rectal gas, which leads to banding artifacts located very close to the rectal wall or inside the prostate. Based on an example of one patient with rectal gas, we expect FMs to be distinctly visualized in all acquired images with artifact pattern similar to the one predicted by simulations. An additional advantage of the use of phase-cycling is that the banding artifacts spatially shift for different RF phase increments allowing always an observation where the banding artifacts do not coincide with the FMs.

For this pulse sequence, TE is always chosen equal to TR/2. As we showed, the choice of TR has a very minor effect on the appearance of the artifacts, which allows for adjustment of TR (and correspondingly TE) for any specific purpose, such as to save scanning time by decreasing TR or to acquire fat-water in-phase or out-of-phase images by adjusting TE.

The acquisition time is proportional to the number of dynamics used. In our experiments, we used the RF phase-cycling scheme with 6 RF phase increment settings, which resulted in the acquisition time of around 2 min. However, the number of RF phase increment settings can be further reduced to 4 or even less to save scanning time.

The manifestations of the artifacts around FMs in phase-cycled bSSFP images depend on the RF phase increment and are different for each dynamic acquisition, which creates a specific pattern of artifacts. This knowledge can be further used for template matching algorithms, which may increase the accuracy of automatic FMs localization methods, at the cost of needing post-processing software.

The results show accurate (within 1 mm) matching of FMs localization between CT and MR images on five patients, proving the feasibility of *in vivo* FMs detection on MR images only.

Our results show that in the real/imaginary images of the dynamics number 5 and number 6, the prostate manifests itself as a strongly hypo-intense structure with very good contrast with neighboring tissues. In the future, we will investigate whether this technique could be used for prostate contouring as well. A multi-purpose sequence for contouring and FMs localization is desirable as for separate scans there is always the risk of inter-scan motion that will propagate as a systematic error in the position of the prostate. Additionally, the use of a multi-purpose sequence would reduce the overall examination time, which is clinically beneficial.

## 5. Conclusion

We have presented a new method for direct visualization of fiducial markers in the prostate for MRI-only radiotherapy. The method is based on phase-cycled bSSFP imaging, providing different contrast of FMs with background dependent on RF phase increment used. The method does not require any additional post-processing or software. Thereby, detection of FMs can be easily done directly at the MR console, allowing RT technicians to obtain immediate feedback on the anticipated feasibility of accurate FM localization while the patient is being scanned.

## ORCID iDs

Yulia Shcherbakova  <https://orcid.org/0000-0003-3521-1767>

Stefano Mandija  <https://orcid.org/0000-0002-4612-5509>

Ellis Beld  <https://orcid.org/0000-0002-7480-2909>

## References

- Bangerter N K, Hargreaves B A, Vasanaawala S S, Pauly J M, Gold G E and Nishimura D G 2004 Analysis of multiple-acquisition SSFP *Magn. Reson. Med.* **51** 1038–47
- Beld E, Moerland M A, van der Voort van Zyp J R N, Viergever M A, Lagendijk J J W and Seevinck P R 2019 MRI artifact simulation for clinically relevant MRI sequences for guidance of prostate HDR brachytherapy *Phys. Med. Biol.* **64** 95006
- Bieri O and Scheffler K 2013 Fundamentals of balanced steady state free precession MRI *J. Magn. Reson. Imaging* **38** 2–11
- Bojorquez J Z, Bricq S, Acquitier C, Brunotte F, Walker P M and Lalande A 2017 What are normal relaxation times of tissues at 3 T? *Magn. Reson. Imaging* **35** 69–80
- Bol G H, Kotte A N T J, van der Heide U A and Lagendijk J J W 2009 Simultaneous multi-modality ROI delineation in clinical practice *Comput. Methods Programs Biomed.* **96** 133–40
- Brown R W, Cheng Y C N, Haacke E M, Thompson M R and Venkatesan R 2014 *Magnetic Resonance Imaging: Physical Principles and Sequence Design* 2nd edn (New York: Wiley)
- Chan M F, Cohen G N and Deasy J O 2015 Qualitative evaluation of fiducial markers for radiotherapy imaging *Technol. Cancer Res. Treat.* **14** 298–304
- Crook J M, Raymond Y, Salhani D, Yang H and Esche B 1995 Prostate motion during standard radiotherapy as assessed by fiducial markers *Radiother. Oncol.* **37** 35–42
- Dehnad H, Nederveen A J, Van Der Heide U A, Van Moorselaar R J A, Hofman P and Lagendijk J J W 2003 Clinical feasibility study for the use of implanted gold seeds in the prostate as reliable positioning markers during megavoltage irradiation *Radiother. Oncol.* **67** 295–302
- Dong Y, Chang Z, Xie G, Whitehead G and Ji J X 2015 Susceptibility-based positive contrast MRI of brachytherapy seeds *Magn. Reson. Med.* **74** 716–26
- Habermehl D, Henkner K, Ecker S, Jäkel O, Debus J and Combs S E 2013 Evaluation of different fiducial markers for image-guided radiotherapy and particle therapy *J. Radiat. Res.* **54** i61–8
- Hargreaves B A, Worters P W, Pauly K B, Pauly J M, Koch K M and Gold G E 2011 Metal-induced artifacts in MRI *Am. J. Roentgenol.* **197** 547–55
- Herman M G, Pisansky T M, Kruse J J, Prisciandaro J I, Davis B J and King B F 2003 Technical aspects of daily online positioning of the prostate for three-dimensional conformal radiotherapy using an electronic portal imaging device *Int. J. Radiat. Oncol. Biol. Phys.* **57** 1131–40
- Hong C G, Yoon B I, Choe H S, Ha U S, Sohn D W and Cho Y H 2012 The prevalence and characteristic differences in prostatic calcification between health promotion center and urology department outpatients *Korean J. Urol.* **53** 330–4
- Jonsson J H, Garpebring A, Karlsson M G and Nyholm T 2012 Internal fiducial markers and susceptibility effects in MRI—simulation and measurement of spatial accuracy *Int. J. Radiat. Oncol. Biol. Phys.* **82** 1612–8
- Khoo V S, Dearnaley D P, Finnigan D J, Padhani A, Tanner S F and Leach M O 1997 Magnetic resonance imaging (MRI): considerations and applications in radiotherapy treatment planning *Radiother. Oncol.* **42** 1–15
- Kim J, Glide-Hurst C, Doemer A, Wen N, Movsas B and Chetty I J 2015 Implementation of a novel algorithm for generating synthetic CT images from magnetic resonance imaging data sets for prostate cancer radiation therapy *Int. J. Radiat. Oncol. Biol. Phys.* **91** 39–47
- Koch K M, Hargreaves B A, Pauly K B, Chen W, Gold G E and King K F 2010 Magnetic resonance imaging near metal implants *J. Magn. Reson. Imaging* **32** 773–87
- Korhonen J, Kapanen M, Keyriläinen J, Seppälä T and Tenhunen M 2014 A dual model HU conversion from MRI intensity values within and outside of bone segment for MRI-based radiotherapy treatment planning of prostate cancer *Med. Phys.* **41** 011704
- Lauzon M L and Frayne R 2009 Analytical characterization of RF phase-cycled balanced steady-state free precession *Concepts Magn. Reson. A* **34A** 133–43
- Lee Y K, Bollet M, Charles-Edwards G, Flower M A, Leach M O, McNair H, Moore E, Rowbottom C and Webb S 2003 Radiotherapy treatment planning of prostate cancer using magnetic resonance imaging alone *Radiother. Oncol.* **66** 203–16
- Mani V, Briley-Saebo K C, Itskovich V V, Samber D D and Fayad Z A 2006 Gradient echo Acquisition for Superparamagnetic particles with Positive contrast (GRASP): sequence characterization in membrane and glass superparamagnetic iron oxide phantoms at 1.5T and 3T *Magn. Reson. Med.* **55** 126–35
- Maspero M 2018 Magnetic resonance-only radiotherapy for prostate cancer *PhD Thesis* Utrecht University, The Netherlands
- Maspero M, Seevinck P R, Schubert G, Hoesl M A U, Van Asselen B, Viergever M A, Lagendijk J J W, Meijer G J and Van Den Berg C A T 2017b Quantification of confounding factors in MRI-based dose calculations as applied to prostate IMRT *Phys. Med. Biol.* **62** 948–65
- Maspero M, Seevinck P R, Willems N J W, Sikkas G G, de Kogel G J, de Boer H C J, van der Voort van Zyp J R N and van den Berg C A T 2018 Evaluation of gold fiducial marker manual localisation for magnetic resonance-only prostate radiotherapy *Radiat. Oncol.* **13** 105

- Maspero M, Van Den Berg C A T, Zijlstra F, Sikkes G G, De Boer H C J, Meijer G J, Kerkmeijer L G W, Viergever M A, Lagendijk J J W and Seevinck P R 2017a Evaluation of an automatic MR-based gold fiducial marker localisation method for MR-only prostate radiotherapy *Phys. Med. Biol.* **62** 7981–8002
- Nederveen A, Lagendijk J and Hofman P 2000 Detection of fiducial gold markers for automatic on-line megavoltage position verification using a marker extraction kernel (MEK) *Int. J. Radiat. Oncol. Biol. Phys.* **47** 1435–42
- Ng M, Brown E, Williams A, Chao M, Lawrentschuk N and Chee R 2014 Fiducial markers and spacers in prostate radiotherapy: Current applications *BJU Int.* **113** 13–20
- Nyholm T, Nyberg M, Karlsson M G and Karlsson M 2009 Systematisation of spatial uncertainties for comparison between a MR and a CT-based radiotherapy workflow for prostate treatments *Radiat. Oncol.* **4** 54–62
- Parker C C, Damyanovich A, Haycocks T, Haider M, Bayley A and Catton C N 2003 Magnetic resonance imaging in the radiation treatment planning of localized prostate cancer using intra-prostatic fiducial markers for computed tomography co-registration *Radiother. Oncol.* **66** 217–24
- Roberson P L, McLaughlin P W, Narayana V, Troyer S, Hixson G V and Kessler M L 2005 Use and uncertainties of mutual information for computed tomography/magnetic resonance (CT/MR) registration post permanent implant of the prostate *Med. Phys.* **32** 473–82
- Seevinck P R, de Leeuw H, Bos C and Bakker C J G 2011 Highly localized positive contrast of small paramagnetic objects using 3D center-out radial sampling with off-resonance reception *Magn. Reson. Med.* **65** 146–56
- Seppenwoolde J H, Viergever M A and Bakker C J G 2003 Passive tracking exploiting local signal conservation: the white marker phenomenon *Magn. Reson. Med.* **50** 784–90
- Shcherbakova Y, van den Berg C A T, Moonen C T W and Bartels L W 2019 On the accuracy and precision of PLANET for multiparametric MRI using phase-cycled bSSFP imaging *Magn. Reson. Med.* **81** 1534–52
- Shcherbakova Y, van den Berg C A T, Moonen C T W and Bartels L W 2018 PLANET: An ellipse fitting approach for simultaneous T1 and T2 mapping using phase-cycled balanced steady-state free precession *Magn. Reson. Med.* **79** 711–22
- Tyagi N, Fontenla S, Zhang J, Cloutier M, Kadbi M, Mechalakos J, Zelefsky M, Deasy J and Hunt M 2017 Dosimetric and workflow evaluation of first commercial synthetic CT software for clinical use in pelvis *Phys. Med. Biol.* **62** 2961–75
- Xiang Q S and Hoff M N 2014 Banding artifact removal for bSSFP imaging with an elliptical signal model *Magn. Reson. Med.* **71** 927–33
- Zijlstra F, Bouwman J G, Braškutė I, Viergever M A and Seevinck P R 2017 Fast Fourier-based simulation of off-resonance artifacts in steady-state gradient echo MRI applied to metal object localization *Magn. Reson. Med.* **78** 2035–41
- Zur Y, Wood M L and Neuringer L J 1990 Motion-insensitive, steady-state free precession imaging *Magn. Reson. Med.* **16** 444–59